21. M. R. Allen *et al.*, *Surv. Geophys.*, in press.
22. G. C. Hegerl, P. D. Jones, T. P. Barnett, *J. Clim.* **14**, 198 (2001).
23. $r^2 = u^T C_N^{-1} u$, where u is the difference vector between the observation and model data ($y_{obs} - y_{model}$) and C_N^{-1} is the inverse of the climate noise covariance matrix as estimated from segments of AOGCM control simulations. Because only limited length control segments are available, a truncated representation of C_N^{-1} must be used, based on a projection onto the κ leading eigenvectors of the estimated C_N (*21*). We use $\kappa = 14$ for both the surface and upper-air temperature diagnostics, but similar results are obtained for a range of truncations (*5*). As described in (*5*), $\Delta r^2 \sim mF_{m,n}$, where $F_{m,n}$ is the F statistic with m and n degrees of freedom, m is the number of constrained model properties, and n is the degrees of freedom in estimated climate noise. Hence, Δr^2 provides a basis for rejecting climate model simulations as being inconsistent with the simulation with the minimum r^2 value. For a given level of significance, we compute the appropriate F statistic that provides a cutoff value for r^2. If r^2 is above this cutoff value, we reject the hypothesis that the Δr^2 is consistent with estimated climate noise.
24. For the surface and upper-air diagnostics, the climate noise was estimated from the second-generation AOGCM developed at the Hadley Centre for Climate Prediction and Research (HadCM2) (*37*). For the ocean diagnostic, the Geophysical Fluid Dynamics Laboratory AOGCM, GFDL_R30_c (*38*), was used because estimates from HadCM2 were not readily available.
25. T. Bayes, *Philos. Trans. R. Soc.* **53**, 370 (1763).
26. To compute the updated distributions for $p(\Pi|\Delta T)$, we first interpolate the r^2 values onto a finer grid [$\Delta S = 0.1$ K, $\Delta(K_v^{1/2}) = 0.1$ cm/s$^{1/2}$] over the range $S = 0.5$ to 10 K and $K_v = 0.2$ to 64 cm^2/s. After the data were interpolated in the S-K_v plane, we interpolated between the aerosol forcing levels to a resolution of $\Delta F_{aer} = 0.05$ W/m^2 over the range 0 to 1.5 W/m^2. After the r^2 values were interpolated, the probability of rejection was estimated (*23*) to generate the probability distribution on the finer grid. For all integral estimates of total probability or marginal probability distributions, the finer grid spacing was used over the ranges specified.
27. The ranges explored for the model parameters set the limits of the uniform priors: $S = 0.5$ to 10 K, $K_v = 0.2$ to 64 cm^2/s, and $F_{aer} = -1.5$ to 0 W/m^2. We can assess the impact of these priors by examining the posterior distributions.
28. T. P. Barnett, D. W. Pierce, R. Schnur, *Science* **292**, 270 (2001).
29. S. Levitus *et al.*, *Science* **292**, 267 (2001).
30. Marginal pdf(Π_i) $\equiv \int p(\Pi) d\Pi_j$, where Π_i is the ith parameter and $D_{j \neq i}$ is the parameter-space domain not including i.
31. M. D. Webster, A. P. Sokolov, *Clim. Change* **46**, 417 (2000).
32. U. Cubasch *et al.*, in *Climate Change 2001, The Scientific Basis*, J. T. Houghton *et al.*, Eds. (Cambridge Univ. Press, Cambridge, 2001), pp. 525–582.
33. J. M. Gregory, *Clim. Dyn.* **16**, 501 (2000).
34. J. Hansen *et al.*, *J. Geophys. Res.*, in press.
35. T. M. L. Wigley, S. C. B. Raper, *Nature* **344**, 324 (1990).
36. S. C. B. Raper, J. Gregory, R. S. Stouffer, *J. Clim.* **15**, 124 (2002).
37. T. C. Johns *et al.*, *Clim. Dyn.* **13**, 103 (1997).
38. T. R. Knutson, T. L. Delworth, K. W. Dixon, R. J. Stouffer, *J. Geophys. Res.* **104**, 30981 (1999).
39. We thank N. Gillett for streamlining the fingerprint detection code, T. Delworth for GFDL_R30_c ocean data, J. Antonov for deep-ocean temperature data, the Hadley Centre for Climate Prediction and Research for HadCM2 data, and A. Slinn for her graphics expertise. This work was supported by a National Oceanic and Atmospheric Administration Office of Global Programs grant NA06GP0061 (C.E.F.) and the European Commission QUARCC project (M.R.A.). The control run of HadCM2 was funded by the UK Department of the Environment, Transport, and Regions under contract number PECD 7/12/37.

16 July 2001; accepted 14 November 2001

Intracellular Iron Minerals in a Dissimilatory Iron-Reducing Bacterium

Susan Glasauer,* Sean Langley, Terry J. Beveridge

Among prokaryotes, there are few examples of controlled mineral formation; the formation of crystalline iron oxides and sulfides [magnetite (Fe_3O_4) or greigite (Fe_3S_4)] by magnetotactic bacteria is an exception. *Shewanella putrefaciens* CN32, a Gram-negative, facultative anaerobic bacterium that is capable of dissimilatory iron reduction, produced microscopic intracellular grains of iron oxide minerals during growth on two-line ferrihydrite in a hydrogen-argon atmosphere. The minerals, formed at iron concentrations found in the soil and sedimentary environments where these bacteria are active, could represent an unexplored pathway for the cycling of iron by bacteria.

Many of the metabolic pathways affecting mineral-bacterium interactions in anaerobic subsurface environments are poorly defined, despite their potential impact on the lithosphere and hydrosphere. Metal-reducing *Shewanella* spp. are known to use mineral-bound Fe(III) [e.g., Fe (hydr)oxides] as the terminal electron acceptor for the membrane-bound electron transport chain during respiration, and Fe^{2+} from the reduction forms extracellular fine-grained minerals (*1*). Little is known about changes to the cell and its structure during the reduction of Fe(III) minerals; investigators often use readily soluble organo-Fe(III) complexes (e.g., Fe-citrate), rather than Fe(III) minerals, for metabolic studies on Fe reduction [e.g., (*2*)] because these allow easy isolation of cells without their problematic separation from the granular mineral matrix. Growth on soluble Fe could, however, be quite different from growth on particulate Fe(hydr)oxides, where the substrate is more tenaciously bound. Tracking the fate of the Fe^{2+} produced during dissimilatory reduction of Fe(III) minerals requires the monitoring of changes in the cell during growth as well as in the minerals produced. Such a study can elucidate the pathways of Fe and its toxic analogs (e.g., U, Tc, and Cr) in natural systems, where Fe minerals can be abundant but Fe chelates are rare (*3*).

Cells of *S. putrefaciens* CN32 were grown in a defined medium (*1*, *4*). The initial cell density was 2×10^7 colony-forming units (CFU)/ml, which rapidly decreased to 6×10^6 CFU/ml during the first day and slowly cycled at this level for 2 weeks before declining again. A plateau in CFU/ml was eventually reached, indicating that cells remained active and viable, replacing themselves as others died so that a steady state was reached. This slow growth reflected the relatively poor nutrient conditions relative to traditional batch culture methods.

Hydrous ferric oxide [termed two-line ferrihydrite because of the two broad diffraction lines seen by x-ray diffraction (XRD) (*5*)] was the electron acceptor. These ~50- to 150-nm fine-grained aggregates of ferrihydrite, when added to the medium, immediately adsorbed to the cells (Fig. 1) and were the source of cellular Fe. The Fe concentrations were representative of natural levels commonly found in marine and soil sedimentary environments (*6*, *7*). Significant Fe^{2+} (relative to an uninoculated control) was detected after 1 to 4 days by the ferrozine method (*8*), and Fe^{2+} increased for ~2 weeks before decreasing slowly (Fig. 2). Intracellular fine-grained (30 to 50 nm) granules were first observed by transmission electron microscopy (TEM) 3 to 5 days after inoculation and were never seen before the appearance of Fe^{2+} in the reaction mixture (*9*). By 14 days, the proportion of cells with visible granules had increased to >90% of the population,

Table 1. Electron diffraction data for crystalline intracellular particles formed by *S. putrefaciens* CN32.

Standard magnetite* (nm)	Sample (nm)
0.2967 (30)†	
0.2532 (100)	0.2525 (311)‡
0.2424 (8)	
0.2099 (20)	0.2044 (400)
0.1715 (10)	0.1780 (422)
0.1616 (30)	0.1570 (511)
0.1485 (40)	0.1506 (440)
0.1419 (2)	
0.1328 (4)	
0.1281 (10)	0.1301 (533)
0.1266 (4)	
0.1212 (2)	
0.1122 (4)	
0.1093 (12)	0.1040 (731)

*ASTM card 19-629. †Denotes XRD intensity. ‡Denotes *hkl* values.

Department of Microbiology, College of Biological Science, University of Guelph, Guelph, Ontario N1G 2W1, Canada.

*To whom correspondence should be addressed. E-mail: sglasaue@micro.uoguelph.ca

and the granules were clearly concentrated in the cytoplasm at one or both cell poles (Fig. 3). In contrast to the tightly aggregated, irregularly sized and shaped masses of the two-line ferrihydrite, the intracellular granules had a fairly regular polyhedral shape and were more homogeneous (Fig. 1).

In thin section, each intracellular mineral granule appeared to be surrounded by a membrane (Fig. 1B). The determination of the membrane was made difficult because of the so-called "phase" or "out-of-focus" effect often accompanying electron-dense particles visualized by TEM. If such granules are not in exact focus, a ring will appear at the granule's periphery that artificially suggests the presence of a bilayered membrane. For this reason, two series of images were taken: through-focus images to ascertain the presence of a phase effect, and tilted images for stereo viewing to ensure that juxtaposed granules were not contributing to such an effect. All analyses verified the existence of a membrane of similar thickness as the lipid bilayer in magnetosomes (*10*). It is possible that this membrane assists the cell as it manufactures the new intracellular mineral.

The number of granules per cell increased with time. Although accurate counting was difficult (the uppermost ones obscured the view of ones beneath), we estimate that there were as many as 60 granules per cell. They first formed near the plasma membrane and appeared to be pushed into the cytoplasm as subsequent granules developed. Cells containing granules appeared particularly healthy relative to those without them, as judged from the density of the cytoplasm in whole mounts and thin sections. Energy-dispersive spectroscopy (EDS) confirmed that the granules were rich in Fe and O with no other metal or counterions detectable above cellular background levels, except for traces of P (Fig. 4) (*11*), contributed by DNA, RNA, and phospholipid.

After 1 week, selected area electron diffraction (SAED) (*12*) showed that the extracellular minerals, both free and bound to the cells, remained as randomly oriented two-line ferrihydrite, as indicated by the pattern of two distinct rings. Lattice (*d*) spacings at 0.15 and 0.25 nm agreed well with published results (*13*). The intracellular granules also showed two rings centered at 0.15 and 0.25 nm that overlapped the rings contributed by the carbon-coated Formvar support film and were somewhat broader and more diffuse than for the extracellular mineral. Similar broad rings have been reported for a hydrous ferric oxide phase found within the abdominal cells of honeybees, which contain abundant Fe-rich granules 0.1 to 0.9 μm in diameter (*14*). A small fraction (less than 10%) of the granule clusters gave SAED patterns indicative of a mineral in *S. putrefaciens* distinct from hydrous ferric oxide. The reflections established that the mineral was both different from and more crystalline than the hydrous ferric oxide phase; because the mineral was small and unstable in the electron beam, these reflections were faint and difficult to interpret. We repeatedly observed several reflections that were consistent with magnetite or maghemite, which have very similar *d* spacings (Table 1; standard data are shown for magnetite only). The patterns differed from those typical for extracellular biogenic magnetite formed during Fe reduction, which show random orientation of the tiny (<10 nm) magnetite grains (*1*). Neither were the patterns identical to those we observed with bacterial magnetite from the magnetotactic bacterium MV-1 (*15*). It is difficult to form a clear diffraction image through the bacterial membrane; in the case of the intracellular granules, imaging was complicated by the extremely small size and clustering of the minerals to one cellular location (i.e., the poles), as well as by the presence of extracellular minerals that could not be separated from the cells. For these reasons we cannot accurately identify the intracellular mineral at this time, although the crystallinity of the intracellular granules appeared to be highest in older cultures.

The rate of reduction and amount of intracellular mineral changed with inoculation density. For example, a high inoculum (10^9

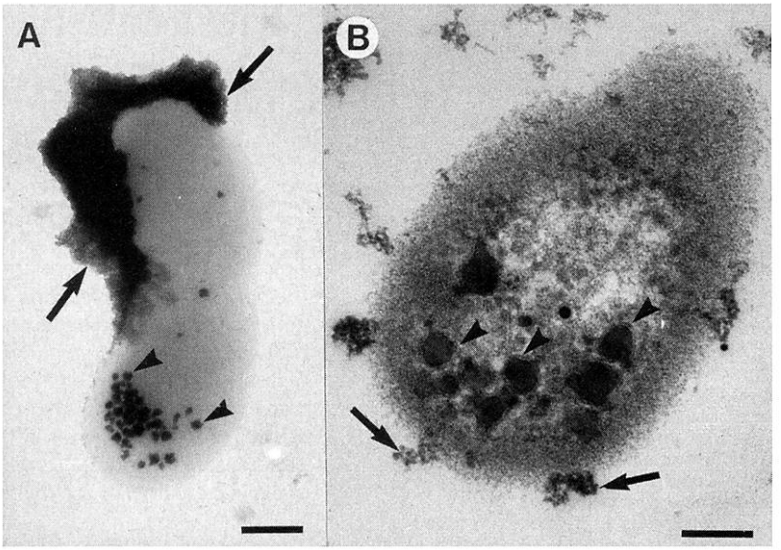

Fig. 1. TEM images of *S. putrefaciens* CN32 cells showing sorbed extracellular two-line ferrihydrite (arrows) and intracellular granules of an iron oxide mineral phase (arrowheads) formed during anaerobic growth. (**A**) Cell prepared for viewing as an unstained whole mount under a H_2/Ar atmosphere. Scale bar, 250 nm. (**B**) Cell in cross section, showing membranes associated with the intracellular particles. Scale bar, 100 nm.

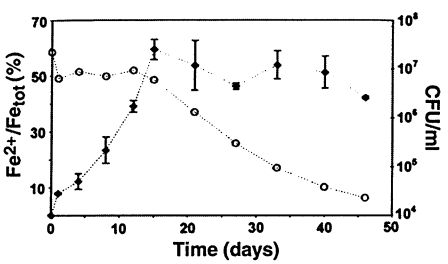

Fig. 2. Change in Fe^{2+} as a percentage of total Fe (closed diamonds) and change in cell numbers (open circles), expressed as CFU/ml, over time for anaerobic liquid cultures of *S. putrefaciens* CN32 during growth in a defined medium with two-line ferrihydrite.

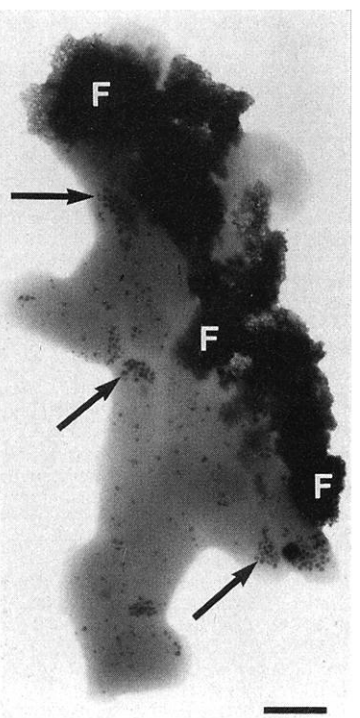

Fig. 3. TEM image showing a whole mount of *S. putrefaciens* CN32 cells associated with extracellular two-line ferrihydrite (F). Note the concentration of granules at the cell polar regions (arrows). Scale bar, 0.5 μm.

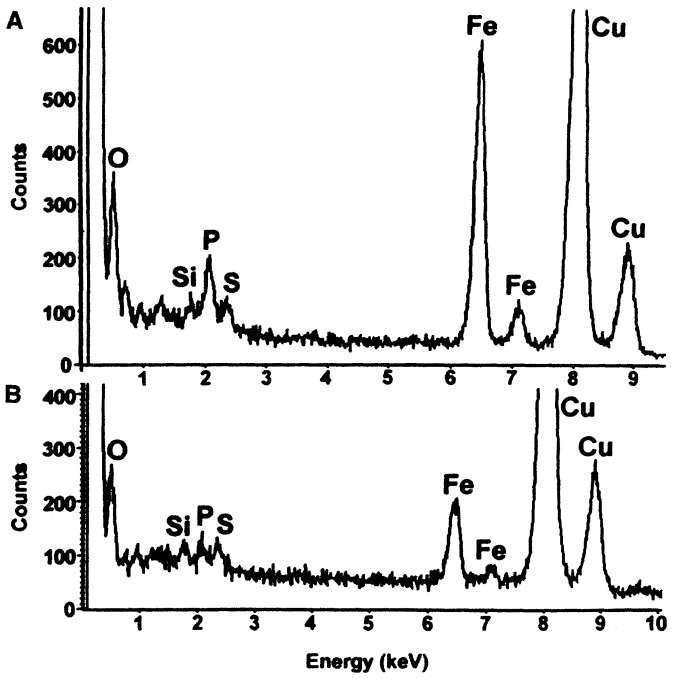

Fig. 4. (A) Energy-dispersive x-ray spectrum from an intracellular granule formed by *S. putrefaciens* CN32, showing peaks for Fe, O, Si, P, Cu, and S. (B) Background spectrum from a granule-free portion of the cell, with the same vertical full scale as for (A). Silicon is derived from the culture glassware; the large copper peaks are from the copper EM grid. The spectra were collected from unstained thin sections.

CFU/ml; same external ferrihydrite concentration; 5 to 8 mM Fe) resulted in higher reduction rates and fewer granules formed per cell (5 to 10 granules) compared to initial results. Varying the concentration of Fe affected the iron reduction rate and the appearance of granules. Because these external factors do not alter internal Fe granule formation, their intracellular deposition could be tightly regulated and integral to cellular metabolism when grown on Fe minerals.

As cells accumulated intracellular granules, new crystalline and poorly crystalline mineral phases were observed to form outside the cells. The variety of different minerals, resolved by XRD and SAED, indicates that the overall Fe chemistry was dynamic and variable throughout the experiment. We detected green rust, magnetite, vivianite, goethite, and poorly crystalline Fe phases between day 7 and day 46, at which time highly crystalline vivianite [$Fe_3(PO_4)_2 \cdot 8H_2O$] predominated (*16*). Of these minerals, only ferrihydrite was detected in the abiotic control, which suggests that cells regulate the Fe geochemistry.

Cells failed to grow when the Fe(III) minerals goethite (α-FeOOH) and hematite (α-Fe_2O_3) replaced ferrihydrite, as shown by a continuous decrease in CFU/ml counts from the time of inoculation. In these cases, no Fe reduction took place and no internal Fe granules were seen. Similarly, no granules formed in cells when fumarate replaced ferrihydrite as the electron acceptor, or when cells were grown under aerobic conditions.

The presence of extracellular magnetite, both in the bulk matrix and sorbed to the cell, prevented us from determining whether the inclusions were magnet-sensitive. The magnet-sensitive properties of a variety of organisms within the Proteobacteria, a group that includes *Shewanella*, were attributed to intracellular structures after cells were grown at high concentrations of soluble Fe (*17*). These structures are nonetheless very different from those we observed with respect to appearance, composition, and location within the cell.

At this point in our studies, we can only speculate on the function of the intracellular Fe particles. The size and morphology of the particles argues against an easily accessible storage depot for iron, such as bacterial ferritin (*18, 19*). In the magnetotactic bacteria, the chains of magnetosomes aligned parallel to the cell axis are thought to play a role in cellular navigation (*20, 21*). However, such high concentrations of intracellular magnetic mineral are not necessary to affect organism behavior, as was shown for honeybees (*14, 22*). Magnetosomes are possibly an exception to a generally more profligate use of Fe minerals by cells, either for navigation or for an as yet unknown purpose.

Bacteria are capable of forming a number of inorganic ion-rich particles in their cytoplasm (*23*), yet the ability to form intracellular fine-grained Fe minerals within prokaryotes is remarkably rare (*20, 21*). Because of the importance of iron metabolism in *S. putrefaciens* CN32, it is possible that the internal Fe oxide granules we detected are essential for growth or are by-products of growth.

References and Notes

1. J. K. Fredrickson *et al.*, *Geochim. Cosmochim. Acta* **62**, 3239 (1998).
2. C. R. Meyers, J. M. Meyers, *FEMS Microbiol. Lett.* **108**, 15 (1993).
3. K. Straub, M. Benz, B. Schink, *FEMS Microbiol. Ecol.* **34**, 181 (2001).
4. We grew *S. putrefaciens* CN32 to mid- to late exponential growth phase in a defined medium (DM) consisting of mineral salts, phosphate, Pipes, and lactate (as an electron donor) under aerobic conditions (*3*). The cells were then washed, gassed with H_2/Ar (4:96), and grown in DM to which enough sterile ferrihydrite suspension was added as the electron acceptor to produce 4 to 8 mM Fe under strict anaerobic conditions at 22°C.
5. Ferrihydrite was precipitated by rapidly adding 1 M NaOH to 0.4 M $FeCl_3 \cdot 6\ H_2O$ until pH 7.0 was reached under sterile conditions, then washed in sterile deionized water. Powder XRD scans were performed on dried crushed samples, using a Rigaku Geigerflex horizontal goniometer, under the following conditions: Co Kα radiation, 45 kV, 25 mA, and 10 s per step with a step size of 0.02°(2θ). Two broad reflections centered at 0.15 and 0.25 nm were observed, and no other mineral phases were detected.
6. R. M. Cornell, U. Schwertmann, *The Iron Oxides: Structure, Properties, Reactions, Occurrence and Uses* (VCH, Weinheim, Germany, 1996).
7. B. Thamdrup, *Adv. Microbiol. Ecol.* **16**, 41 (2000).
8. L. L. Stookey, *Anal. Chem.* **42**, 779 (1970).
9. TEM was performed on a Philips EM300 operating at 60 kV under standard conditions.
10. Y. A. Gorby, T. J. Beveridge, R. P. Blakemore, *J. Bacteriol.* **170**, 834 (1988).
11. EDS was performed on a Hitachi H7110 TEM operating in scanning TEM (STEM) nanoprobe mode and equipped with a Noran Voyager germanium detector. The spot size was 50 nm at 75 kV with a beam current of 25 mA.
12. SAED was performed on whole mounts of cells on carbon- and Formvar-coated Cu grids that were held in a H_2/Ar atmosphere until they were loaded into the microscope. A Philips EM400T (operating at 80 kV with a spot size of 50 nm, camera length of 574 mm, and an exposure time to record reflections of 20 s) and a LEO 912AB (operating at 100 kV with spot size 50 nm, camera length 580 nm, and exposure time 30 s) were used over the course of the experiment.
13. D. E. Janney, J. M Cowley, P. R. Busek, *Am. Mineral.* **85**, 1180 (2000).
14. D. A. Kuterbach, B. Walcott, R. J. Reeder, R. B. Frankel, *Science* **218**, 695 (1982).
15. MV-1 cells, provided by D. Bazylinski, were prepared as for *S. putrefaciens*; SAED was carried out on a LEO 912AB (*14*).
16. Powder XRD was performed on precipitates that were washed, dried, lightly crushed, and packed under a H_2/Ar atmosphere, then scanned as described (*9*) in a N_2 atmosphere.
17. M. B. Vainshtein, N. E. Suzina, E. B. Kudryashova, E. V. Ariskina, V. V. Sorokin, *Microbiology* **67**, 670 (1998) (translated from *Mikrobiologiya*).
18. E. R. Bauminger *et al.*, *Biochim. Biophys. Acta* **623**, 237 (1980).
19. E. I. Steifel, G. D. Watt, *Nature* **279**, 81 (1979).
20. D. A. Bazylinski, B. R. Heywood, S. Mann, R. B. Frankel, *Nature* **366**, 218 (1993).
21. D. A. Bazylinski *et al.*, *Appl. Environ. Microbiol.* **61**, 3232 (1995).
22. J. L. Gould, J. L. Kirschvink, K. S. Deffeyes, *Science* **210**, 1026 (1978).
23. T. J. Beveridge, In *Bacteria in Nature: A Treatise*, E. R. Leadbetter, J. S. Poindexter, Eds. (Plenum, New York, 1989), vol. 3, pp. 1–65.

24. We thank R. Harris, A. Moore, and D. Moyles for TEM and EDS; D. Bazylinski for providing MV-1; Y. Gorby for advice and encouragement; and P. Weidler for constructive comments. Supported by a U.S. Department of Energy Natural and Accelerated Bioremediation Research grant (T.J.B.). TEM and SAED were performed in the Natural Sciences and Engineering Research Council of Canada (NSERC) Guelph Regional STEM Facility, University of Guelph, which is partially supported by a NSERC Major Facility Access grant (T.J.B.).

26 September 2001; accepted 6 November 2001